International Journal of Automotive Technology, Vol. 21, No. 6, pp. 1391–1399 (2020)
DOI 10.1007/s12239–020–0131–7

pISSN 1229–9138/ eISSN 1976–3832

DESIGN OF TRACTION MOTOR FOR MITIGATING ENERGY CONSUMPTION OF LIGHT ELECTRIC VEHICLE CONSIDERING MATERIAL PROPERTIES AND DRIVE CYCLES

Dong-Min Kim, Young-Hoon Jung, Kyoung-Soo Cha and Myung-Seop Lim*

Department of Automotive Engineering, Hanyang University, Seoul 04763, Korea

(Received 23 April 2019; Revised 16 December 2019; Accepted 20 January 2019)

ABSTRACT–Light electric vehicles (LEVs) are usually used as neighborhood electric vehicles (NEVs) for the second vehicle or car-sharing service. For LEVs, it is important to reduce energy consumption to have greater mileage at the same battery capacity. One of the direct ways to decrease energy consumption is the efficiency improvement of the traction motor, which is the main propulsion system. Also, the weight reduction of the traction motor can be a solution to energy usage mitigation. This paper suggested the design process of a traction motor for LEV considering material properties to minimizing the energy consumption of the vehicle. During the design process, vehicle simulation was adopted to calculate energy consumption. In addition, traction motor and battery which are the key components of LEV were mathematically modeled and used in the simulation. Using them, energy consumption was estimated within the change of stack length of the traction motor for some drive cycles. Finally, from these simulations, optimum power density is determined which minimizes energy consumption.

KEY WORDS : Drive cycle, energy consumption, interior permanent magnet synchronous motor (IPMSM), light electric vehicle (LEV), mechanical stress, power density

1. INTRODUCTION

These days, plug-in hybrid electric vehicle (PHEV) and electric vehicles (EVs) are registered more than 1.5 million worldwide (Rahman and Hiti, 2017). In addition, the number of research papers on EV in 2019 is more than 14 times than in 2008 (Search Term: Electric Vehicle, 2019). Recently, the light electric vehicle (LEV) is getting attention according to the trend of transportation electrification. The purpose of LEV is diverse from the used for neighborhood electric vehicle (NEV) as the second vehicle to the used for car-sharing service. Especially in LEVs, it is important to reduce energy consumption to have greater mileage at the same battery capacity. The reason for this is that in the case of LEV, the battery capacity is usually to be small (12 ~ 30 kWh) so that the battery can be frequently exposed to charge/ discharge situation (Grunditz and Thiringer, 2016). And if the energy efficiency is increased, the number of times of charging/discharging can be reduced, and battery life can be expected to increase. Particularly, the car-sharing service with LEV can be applied in the vehicle to grid (V2G) environment (Liu *et al*., 2018; Jafari *et al*., 2018; Kalathil *et al*., 2019). In this situation, the slight energy consumption reduction of each LEV can be a big effect on the whole grid aspect.

To increase the energy efficiency of the EV, the overall weight of the vehicle should be reduced, and the power efficiency for the operating region should be improved. Moreover, reduction of the energy loss should be achieved such as drag coefficient reduction. Especially, what can be done to achieve a reduction of the energy loss in the design aspect of the traction motor, is the improvement of power efficiency and enhancement of the power density of the main propulsion system. There are many studies on the improving efficiency, and power density of traction motor for EV have been carried out.

Momen *et al*. (2019) designed electric motor using hair-pin winding which can secure more slot fill factor. Wu *et al*. (2018) conducted efficiency optimization of interior permanent magnet synchronous motor (IPMSM) considering controller circuit. Hwang *et al*. (2018) studied power density improvement of rare earth free wound field synchronous motor (WFSM) by the permanent magnet (PM) assisting. There are also existed research on the efficiency improvement for the flux modulation machines, not a conventional permanent magnet synchronous motor (PMSM) (Zhao *et al*., 2019; Xiang *et al*., 2019). In addition, papers exist, focusing the efficiency enhancement through the control aspects. Huang *et al*. (2019) studied the torque distribution technique, improving the overall efficiency of the vehicle. Heydari *et al*. (2019) suggested

**Corresponding author*. e-mail: myungseop@hanyang.ac.kr

control strategy which is maximizing recovery energy from the regenerative braking.

2. MULTIPHYSICS IMPROVE DESIGN

In this chapter, an improved design is conducted for LEV traction motor considering not only electromagnetic characteristics but also mechanical stresses. The target of improved design is raising efficiency and power density to reduce the energy consumption of LEV. Firstly, a base model is introduced. Subsequently, the loss investigation is performed considering magnetic materials used in traction motor. Moreover, in the manner of reluctance torque enhancement, the number of inserted magnet layer is determined, considering mechanical stress.

2.1. Base model

The base model of the traction motor for LEV is depicted in Figure 1. This is interior permanent magnet synchronous motor (IPMSM) with a U-type inserted magnet. It has 8-poles 48-slots combination with a distribution winding (five-coil pitch). The maximum power is 30 kW with a maximum torque of 72 Nm. The corresponding base speed is 4,000 rpm, and the maximum speed is 10,000 rpm. The detailed specifications are organized in Table 1. This shows that the iron loss should be considered which is proportional to the square of the operating frequency because of its high speed (10,000 rpm) condition. Figure 2 (a) shows the loss analysis result which describes this condition. In addition, reluctance torque should be considered. Figure 2 (b) shows that the ratio between the magnetic torque and the reluctance torque from the 2D FEA at the rated power and maximum speed situations. The amount of reluctance torque is similar or more.

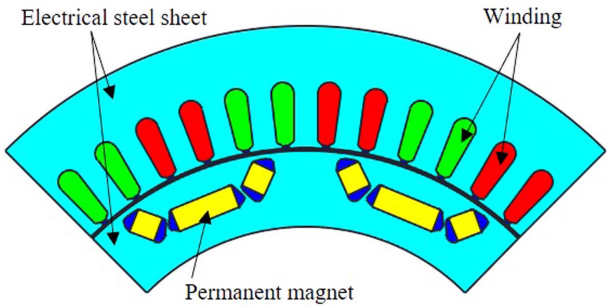

Figure 1. Traction motor construction for LEV.

Table 1. Specification of base model.

Items	Value	Unit
Stator diameter	280	Mm
Rotor diameter	190	Mm
Stack length	42	Mm
Number of poles / slots	8/48	-
DC link voltage	180	V
Base speed	4000	RPM
Maximum speed	10000	RPM
Maximum torque	72	Nm
Maximum power	30	kW

From the analysis results of the base model, copper loss in a high torque operating condition and iron loss in a high speed operating condition should be reduced. In addition, if the saliency ratio can be raised, we could increase the reluctance torque. This allows the motor to increase the torque per current. Therefore, the power density can be increased while simultaneously reducing copper loss and iron loss.

2.2. Electromagnetic design

Electric motors have several losses such as mechanical loss, iron loss and copper loss. The mechanical loss is mainly caused by windage loss and bearing loss. Iron losses from electrical steel sheets are caused by changes in the exposed magnetic field and can be separated into hysteresis losses, eddy current losses, and anomalous loss components. Finally, copper loss is caused by the current flowing through the copper windings. The following paragraphs describe how to reduce iron loss and copper loss.

For the first, the iron loss reduction is explained. The iron losses can be expressed as (1), following Steinmetz's equation, where B is the peak value of the magnetic flux density, α and β are the Steinmetz coefficients, and f is the operating frequency. The coefficients k_h, k_e, and k_a are coefficients of the hysteresis, eddy current, and anomalous losses, respectively (Kim *et al.*, 2019a).

$$W_{iron} = k_h f B^{\alpha} + k_e f^2 B^2 + k_a f^{1.5} B^{\beta} \quad (1)$$

To reduce iron loss, it can be achieved by lowering the peak value of the magnetic flux density or operating frequency. However, high power density and high operating speed are essential for automotive applications. Thus, in this paper, the magnetic core material was

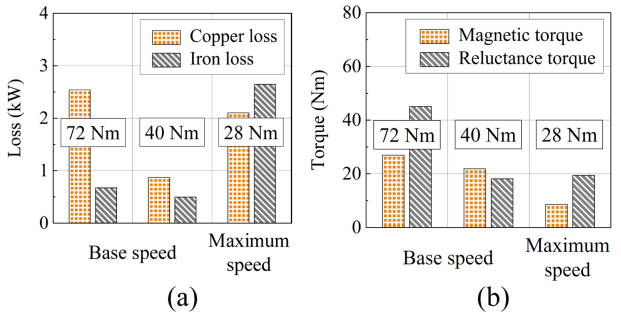

Figure 2. Analysis result of base model (a) losses and (b) portion of magnetic torque and reluctance torque.

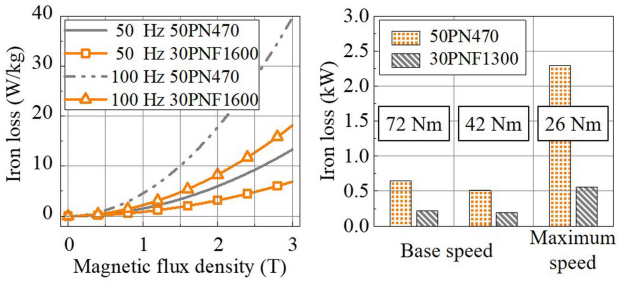

(a) (b)

Figure 3. Electrical steel sheets comparison (a) iron loss and (b) effect on iron loss of electric motor.

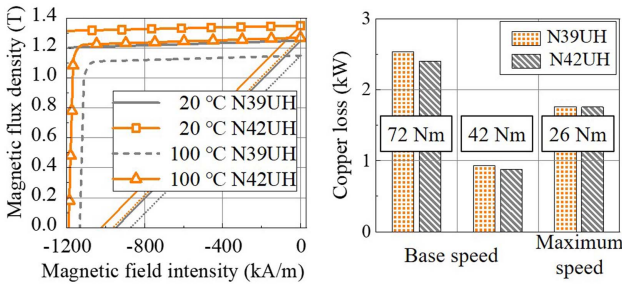

(a) (b)

Figure 4. Permanent magnets comparison (a) B-H curve and (b) effect on copper loss of electric motor.

Table 2. Properties of electrical steel sheets.

Items	Value		Unit
	50PN470	30PNF1600	
W15/50	4.70	2.16	W/kg
Thickness	0.50	0.30	mm
Density	7700	7600	kg/m^3
Yield strength	275	410	MPa
Tensile strength	415	535	MPa
Young's modulus	180	175	GPa
Poisson's ratio	0.30	0.30	-

changed to, which has a lower iron loss, as shown in Figure 3 (a). It means that coefficients k_h, k_e, and k_a are reduced, mentioned above expression as (1). The iron loss per kg of newly adopted electrical steel sheet has 53.3 % lower at 100 Hz where the flux density is 2.0T. Figure 3 (b) shows the effect of the iron loss reduction of the motor due to the change of the electrical steel sheet. The material properties of electrical steel sheets are organized in Table 2.

Next is the explanation for the reduction of copper loss. The copper loss reduction is achieved in many ways. From the well-known equation of output torque of the electric motor is shown in (2), we can guess which parameter increases the output torque. P_n is the number of pole pairs, Ψ_a is the armature linkage flux, I_a is the armature current, β is an armature phase angle, L_q is a q-axis inductance, and L_d is a d-axis inductance. This equation can be thought of as a magnetic torque (3) by the rotor permanent magnet and a reluctance torque (4) by the rotor saliency (Lee *et al.*, 2012).

$$T = P_n \left\{ \Psi_a I_a \cos\beta + \frac{1}{2}(L_q - L_d) I_a^2 \sin 2\beta \right\} \quad (2)$$

$$T_m = P_n \Psi_a I_a \cos\beta \quad (3)$$

Table 3. Properties of permanent magnet.

Items	Value @ 100 °C		Unit
	N39UH	N42UH	
Residual induction	1.15	1.22	T
Coercive force (intrinsic)	1132	1190	kA/m
Recoil permeability	1.05	1.05	-

$$T_r = \frac{1}{2} P_n (L_q - L_d) I_a^2 \sin 2\beta \quad (4)$$

In a given fixed-radius condition, there are several ways to improve power density while improving efficiency. According to (2) ~ (4), suppose that armature is constant, the maximum torque per ampere can be increased by increasing P_n, Ψ_a, or raising the difference between L_q and L_d. The P_n is fixed because the maximum operating speed (10,000 rpm) is high. If the P_n increase, this can be a burden to the inverter because switching frequency should be increased to generate the sinusoidal current waveform. The increment of the Ψ_a can be achieved by increasing the residual induction B_r of permanent magnets, as shown in (5) where the W_m is the magnet width and L_{stk} is the stack length (Matsui *et al.*, 2001; Bianchi and Jahns, 2004).

$$\Psi_a \propto B_r \times W_m \times L_{stk} \quad (5)$$

Figure 4 (a) shows a comparison of magnetic properties according to the permanent magnet grades of N39UH and N42UH. The characteristic values are shown in Table 3. Figure 4 (b) shows the effect of changing the permanent magnet from N39UH to N42UH on copper loss reduction. For the maximum speed condition, the effect is insufficient. However, for the base speed condition, the effect on the copper loss reduction due to the change of PM is considerable.

To raise the difference between q-axis inductance and d-axis inductance, the number of layers of the inserted magnet is analyzed. Ideally, the difference between q-axis

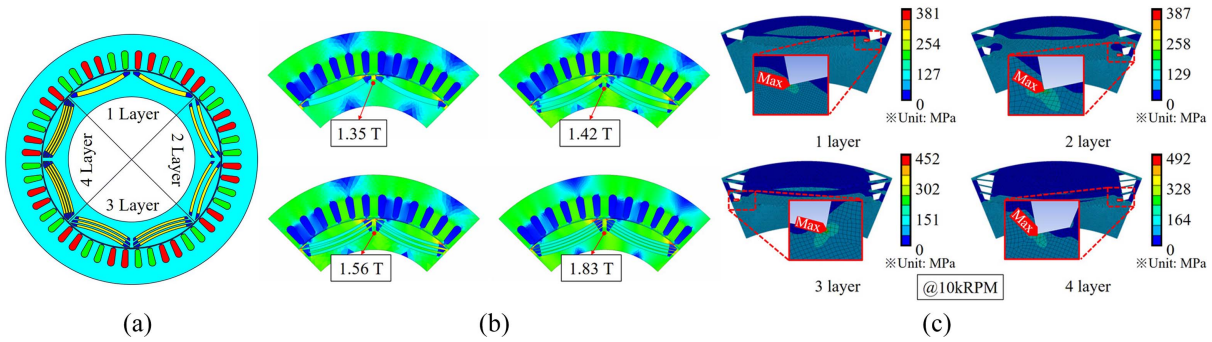

Figure 5. Conceptual models for analyze number of inserted layers (a) geometry, (b) magnetic flux density distribution, and (c) stress distribution.

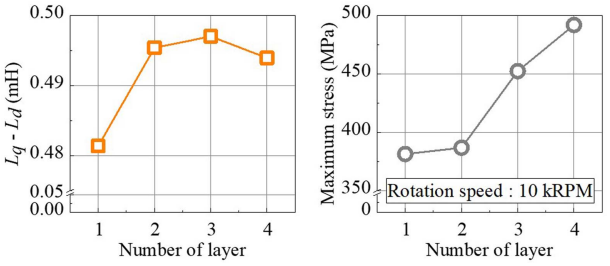

Figure 6. Effect of inserted layer number change on (a) difference between q- and d-axis inductance, and (b) maximum stress of rotor.

inductance and d-axis inductance is increased as the number of magnet layers increases. Because the permeability of magnet is similar to the permeability of air, the number of obstacles in the d-axis flux path is increased as the number of magnet layers increases. To investigate the effect of the number of inserted magnet layers on the difference between inductances, 2D FEA is performed as depicted in Figure 5 (a). The result shows that there exist limits to increment of difference between inductances and it is shown in Figure 6 (a). This result is from the magnetic saturation effect on the q-axis magnetic flux path as described in Figure 5 (b). In the case of 1-layer to 2-layer, the change of inductance difference is the most significant. The 3-layer to 4-layer variation shows a decrease in inductance. Consequently, the candidates for the number of the inserted magnet layers are two and three.

2.3. Mechanical design

In the mechanical design of the electric motor, there are several issues with regard to mechanical stress, heat radiation, and vibration. Especially, for the high speed electric motor, the mechanical stress in the rotor owing to the centrifugal force should be considered. In this chapter, the mechanical stress is analyzed, and a design for mechanical stress reduction is performed.

First, the number of layers of inserted permanent magnets is determined. From the results of section 2.2, the candidates for the number of inserted magnet layers were two and three. Using this model, mechanical stresses are analyzed as von Mises equivalent stresses utilizing ANSYS. Figure 5 (c) shows the mechanical stress simulation results and maximum stress at 10,000 rpm of the maximum rotation speed. The maximum stress increased significantly when the number of magnetic layers was three. As a result, the number of magnetic layers is determined by two.

Next, the inserted magnet division is performed to reduce the maximum mechanical stress to increase the safety factor. As the inserted magnet is segmented, the number of bridges increased. This causes mechanical stress to be distributed to the bridge. The effect of the inserted magnetic segment on mechanical stress reduction is shown in Figure 7. However, segmenting the inserted magnet raised the leakage magnetic flux and decreased the amount of the magnet. As a result, it occurred a decline in electrical

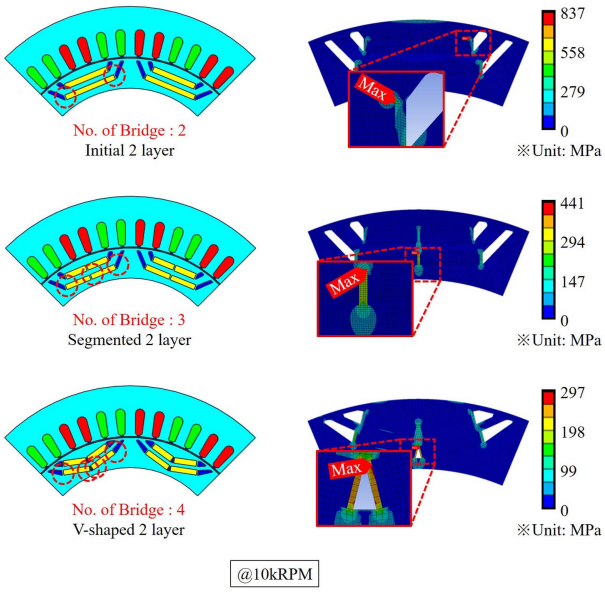

Figure 7. Stress distribution of rotor and maximum stress of rotor according to number of bridge increase.

performance. For these reasons, V-shaped magnets are used to supplement the insufficient amount of permanent magnet. In addition, the difference between *q*- and *d*-axis inductance are slightly increased compared to the non-segmented model. Figure 7 shows the results of inserted V-shaped magnets with bridges and mechanical stress simulations.

2.4. Design result

Figure 8 (a) shows the shape of the base model and the improved model. The maximum efficiency of the improved model is improved from 93.2 % to 96.5 % while maintaining the maximum output power. In addition, the maximum input current is reduced from 179.6 A_{rms} to 168.4 A_{rms}. Figure 10 (a) and (b) show the changes in copper loss and iron loss. The hatched area represents the loss increase, and the other area represents the loss reduction. Figure 10 (c) shows that efficiency is improved for all operating region. In addition, as shown in Figure 8 (b), the safety factor (yield strength divided by maximum stress) increases because the yield strength of changed electrical steel sheets is higher than electrical steel sheets of the base model. The comparison between the base model and the improved model is displayed in Table 4. For the improved model, the demagnetization analysis is conducted as shown in Figure 9. The load condition is determined from the maximum input current with a 20 % margin. The direction is *-d* axis, which is the worst condition (Park *et al*., 2016, Jung *et al*., 2019). There is no difference in linkage flux, it can be assumed that the demagnetization does not occur.

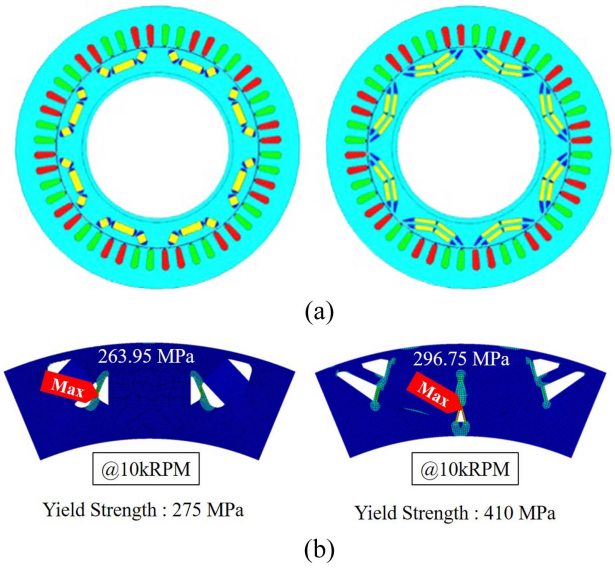

Figure 8. Comparison of base model (left) and improved model (right) (a) shape and (b) safety factor of rotor at 10 kRPM rotating condition.

Table 4. Comparison of base model and improved model.

Items		Value		Unit
		Base	Improved	
Maximum power		30		kW
Maximum torque		72		Nm
Maximum input current		179.6	168.4	A_{rms}
Stator diameter		280		mm
Stack length		42		mm
Weight (include housing)		15.75	15.42	kg
Power density		1.90	1.95	kW/kg
Maximum efficiency		93.2	96.5	%
Mechanical property of rotor	Maximum Stress @10kRPM	263.9	296.8	MPa
	Yield strength	275.0	410.0	GPa
	Safety factor	1.04	1.38	-

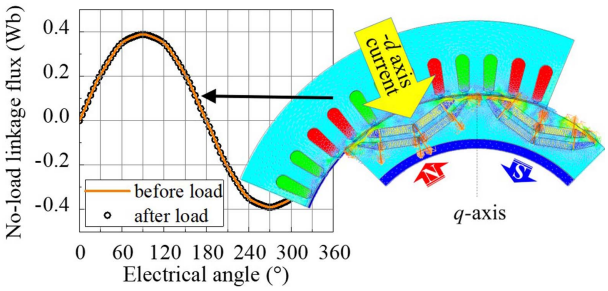

Figure 9. Irreversible demagnetization analysis.

3. LIGHT ELECTRIC VEHICLE MODEL

This chapter introduces vehicle models for vehicle simulation to investigate how the improved model improves energy efficiency. The following descriptions are the LEV specifications, electric motor model and energy storage model.

3.1. Specification

The target vehicle type is EV. The energy storage unit supplies energy to the electric motor, and the power of the electric motor is transferred to the drive system via the reduction gear. The glider mass (curb weight except for drivetrain and energy storage) is assumed as 340 kg, width as 1.19 m, height as 1.46 m, wheelbase as 1.69 m and wheel diameter including tire as 0.53 m. The coefficients related to resistivity are assumed as follows: air density is 1.2 kg/m^3, the drag coefficient is 0.30, and the rolling resistance coefficient is 0.01. Moreover, the gear ratio of reduction gear attached to the traction motor is assumed as 8:1 and its weight is supposed as 20 kg. Detailed specification is organized as Table 5.

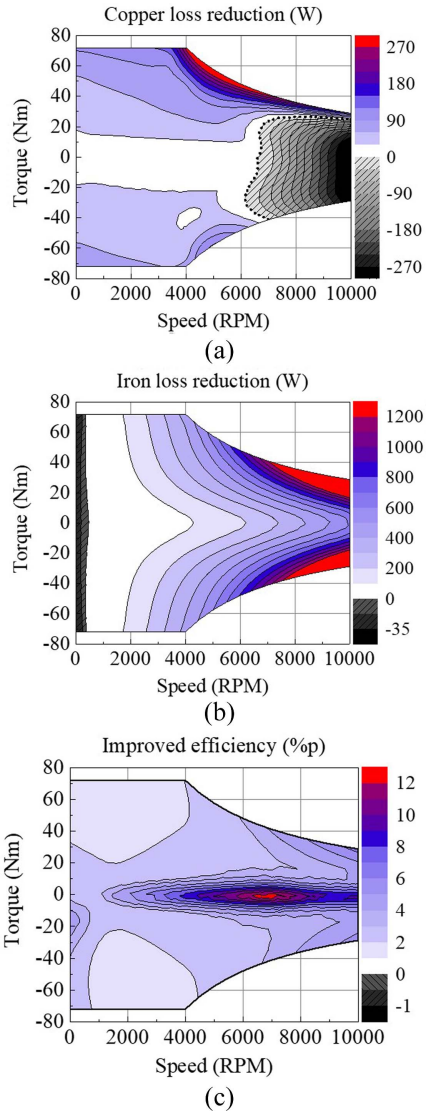

Figure 10. Improved design result (a) copper loss reduction, (b) iron loss reduction and (c) efficiency improvement.

3.2. Traction motor model

To reflect the characteristics of the electric motor, an electric motor model is developed. From Chapter 2, a 2D FEA model was created for each model. One is the base model, and the other is the improved model. Using the 2D FEA, *d-q* axis inductances, linkage flux, and iron losses were obtained for each model according to the operating condition. Especially, iron losses are estimated from FEA result of each element for each step according to Figure 11 (Kim *et al.*, 2019b). Moreover, the phase resistance is calculated from the geometry information, and the copper loss is calculated simultaneously. Subsequently, using the *d-q* axis equivalent circuit, the efficiency map is generated for the whole operating region where the minimum loss control is applied. Figure 12 describes the overall process of developing the electric motor model.

Table 5. Specification of target light electric vehicle.

Items		Value	Unit
Glider weight (except powertrain, battery)		340	kg
Width		1.19	m
Height		1.46	m
Wheelbase		1.69	m
Wheel diameter (include tire)		0.53	m
Rolling resistance coefficient		0.01	-
Air drag coefficient		0.30	-
Air density		1.20	kg/m^3
Reduction gear	Gear ratio	8:1	-
	Weight	20	kg
Battery	Chemistry	$LiFePO_4$	-
	Nominal voltage	189	V
	Nominal capacity	17	kWh
	Weight	136	kg

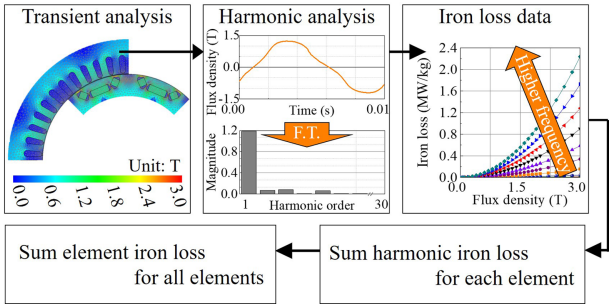

Figure 11. Iron loss calculation process using 2D FEA results.

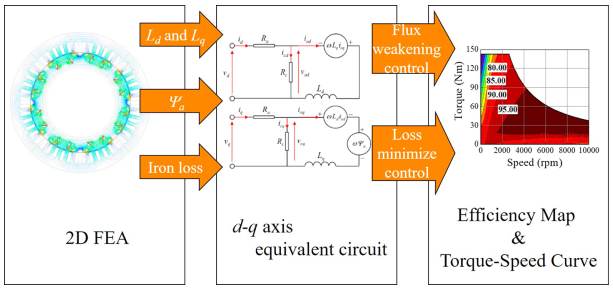

Figure 12. Overall process of electric motor model generation.

3.3. Energy storage model

The lithium-ion (Li-ion) battery is adopted for the energy

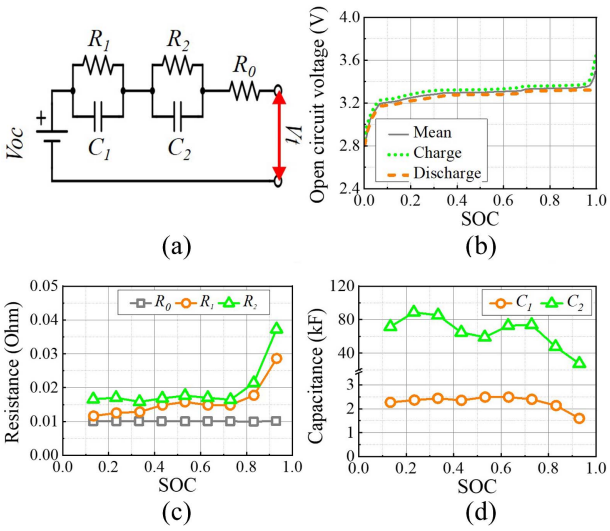

Figure 13. (a) equivalent circuit of energy storage and (b), (c), (d) are corresponding parameters for equivalent circuit according to state of charge.

storage of target EV. Even though the energy density is lower than other chemistry, $LiFePO_4$ chemistry is chosen because of the economic aspect. In this study, a second-order dynamic equivalent model is adopted as shown in Figure 13 (a) (Klein III and Park, 2017; Hu *et al*., 2011). This model is adequate for EV application which is usually exposed to dynamic power requirement (charge/discharge). The matched parameters for this equivalent model are organized in Figure 13 (b) ~ (d). The used SOC calculation method is Coulomb counting. This method is not suitable for long term investigation, considering the state of health (SOH). However, because this research focuses on the relative comparison of energy consumption between the base model and the improved model, there is no problem with using that method accordingly (Xiong *et al*., 2017). The nominal voltage is considered as 189 VDC, and the nominal capacity is assumed as 17 kWh. The mass of a single cell is treated as 70 g, and the package is not considered. As a result, the overall weight is assumed as 136 kg. The information of the energy storage is described in Table 5.

4. VEHICLE SIMULATION RESULT

Using the Advanced Vehicle Simulator (ADVISOR), vehicle simulation is performed. Except for the electric motor and energy storage model, other parts are simulated by utilizing existed models of ADVISOR. In this simulation, the efficiency of reduction gear is assumed as 90 % in constant. Moreover, Artemis drive cycle is adopted for vehicle simulation condition. From the Artemis drive cycles, urban and rural drive cycles are chosen. Figure 14 (a) shows these drive cycles. Their corresponding

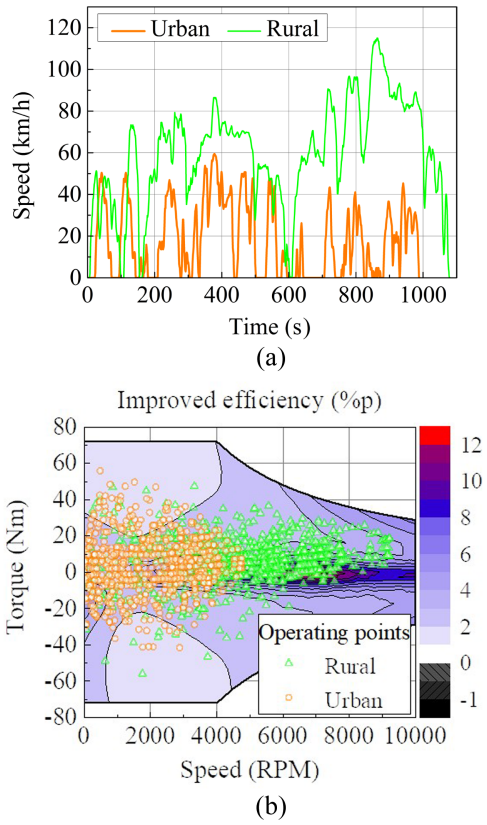

Figure 14. (a) Artemis drive cycles for vehicle simulation and, (b) its corresponding operating points for given conditions.

operating points and efficiency improvement map in % p is depicted in Figure 14 (b). The operating points come from simulation result with the weight of the base model of the traction motor. According to Figure 14 (b), it can be noticed that the urban cycle usually operates the motor at low-speed and high-torque compared to the rural cycle.

Using the vehicle simulation described above, the stack length of the improved model is determined. The aim of this determination is to find out the optimum power density that minimizes energy consumption. Figure 15 (a) shows the weight and corresponding power density along the stack length of the improved model. Obviously, the shorter the stack length, the lighter the weight and the higher the power density. Figure 15 (b) shows that the trend of energy consumption according to each drive cycle as the stack length of the traction motor is change. The weight and efficiency map according to the stack length is considered. The orange line with square symbol depicts the energy consumption of the urban cycle, green line with triangular symbol depicts the energy consumption of the rural cycle, and the gray line with circular symbol depicts energy consumption of total cycle (urban + rural). For the urban drive cycle, the energy consumption is lowest with 42 mm stack length. On the other hands, the energy consumption is lowest with 36 mm stack length. For the total drive cycle,

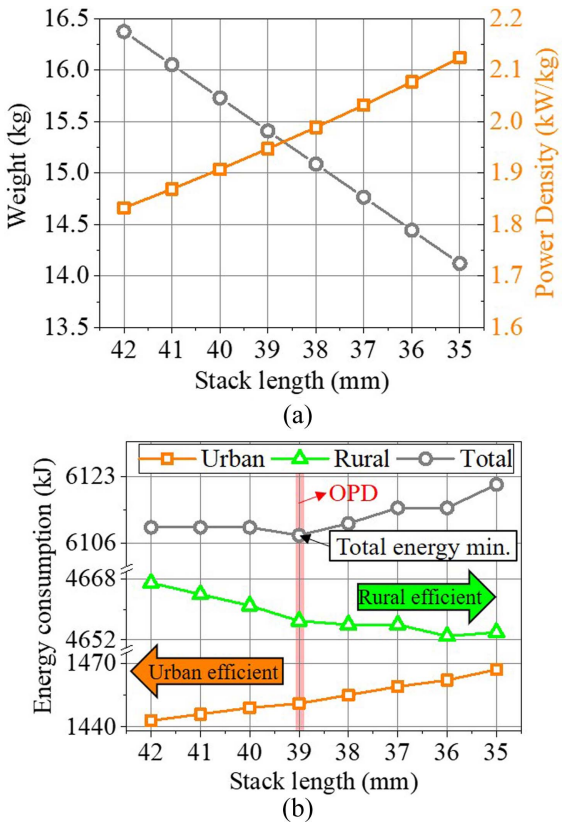

Figure 15. Effect of stack length on (a) electric motor weight and power density, (b) energy consumption results from vehicle simulation.

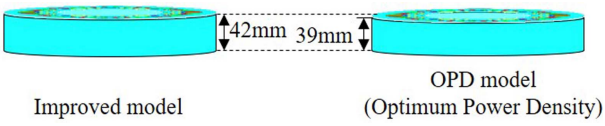

Figure 16. Stack length comparison of improved model and OPD (optimum power density) model.

energy consumption is lowest with 39 mm stack length. In this paper, in order to reduce energy consumption equally for rural and urban cycles, the stack length of the optimum power density (OPD) model is determined as 39 mm. This is illustrated in Figure 15 (b) and comparison with the improved model is shown in Figure 15.

Consequently, Figure 16 describes the overall result of this study. The comparison of power density and energy consumption for the base model, improved model, and OPD model is displayed. When comparing the base model and the OPD model, the power density is improved from 1.90 kW/kg to 2.08 kW/kg (9.5 %), and the energy consumption for total (urban + rural) cycle is reduced from 6414 kJ to 6108 kJ (– 306 kJ), for the urban cycle is reduced from 1501 kJ to 1451 kJ (– 50 kJ), and for the rural cycle is reduced from 4913 kJ to 4657 kJ (– 256 kJ).

5. CONCLUSION

This study presented the design process of traction motor for energy consumption mitigation of LEV. To perform the design, an IPMSM was adopted for the base model. Firstly, for the same size condition of the base model, the improved design was conducted. This was conducted from the investigation of the material properties and the relationship of the output torque equation. Then, vehicle simulation was prepared and conducted to compare energy consumption. For the vehicle simulation, Artemis drive cycle was adopted. Among the Artemis cycles, the urban and the rural cycle was chosen as the target cycle. Finally, using the improved model in the same size condition, vehicle simulations were conducted along change the stack length of the improved model. As a result, there existed the optimum stack length for each drive cycle. In this paper, the optimum stack length for OPD model was determined as the minimizing the energy consumption of the total (urban + rural) cycle. However, if there are applications using only a certain cycle, the optimum power density can be determined for each application. If we follow the design flow of this paper according to the situation, we can determine the optimal power density for a specific purpose.

ACKNOWLEDGEMENT–This work was supported by the National Research Foundation of Korea (NRF) grant funded by the Korea government (MSIP; Ministry of Science, ICT & Future Planning) (No. NRF-2020R1A4A4079701).

REFERENCES

Bianchi, N. and Jahns, T. M. (2004). Design, analysis, and control of interior PM synchronous machines. *Tutorial course notes, IEEE Industry applications society*, Seattle, Washington, USA.

Grunditz, E. A. and Thiringer, T. (2016). Performance analysis of current BEVs based on a comprehensive review of specifications. *IEEE Trans. Transportation Electrification* **2**, **3**, 270–289.

Heydari, S., Fajri, P., Rasheduzzaman, M. and Sabzehgar, R. (2019). Maximizing regenerative braking energy recovery of electric vehicles through dynamic low-speed cutoff point detection. *IEEE Trans. Transportation Electrification* **5**, **1**, 262–270.

Hu, Y., Yurkovich, S., Guezennec, Y. and Yurkovich, B. (2011). Electro-thermal battery model identification for automotive applications. *J. Power Sources* **196**, **1**, 449–457.

Huang, J., Liu, Y. Liu, M. Cao, M. and Yan, Q. (2019). Multi-objective optimization control of distributed electric drive vehicles based on optimal torque distribution. *IEEE Access*, **7**, 16377–16394.

Hwang, S.-W., Sim, J.-H. Hong, J.-P. and Lee, J.-Y. (2018). Torque improvement of wound field synchronous motor for electric vehicle by PM-Assist. *IEEE Trans. Industry*

Applications **54**, **4**, 3252–3259.

Jafari, M., Gauchia, A., Zhao, S., Zhang, K. and Gauchia, L. (2018). Electric vehicle battery cycle aging evaluation in real-world daily driving and vehicle-to-grid services. *IEEE Trans*. *Transportation Electrification* **4**, **1**, 122–134.

Jung, Y.-H., Kim, K.-O. and Hong, J.-P. (2019). Design of multi-layer IPMSM using ferrite PM considering mechanical and electrical characteristics. *2019 IEEE Energy Conversion Cong. and Expo. (ECCE)*, Baltimore, MD, USA, 3534–3541.

Kalathil, D., Wu, C., Poolla, K. and Varaiya, P. (2019). The sharing economy for the electricity storage. *IEEE Trans*. *Smart Grid* **10**, **1**, 556–567.

Kim, D.-M., Chin, J.-W., Hong, J.-P. and Lim, M.-S. (2019a). Performance prediction of surface-mounted permanent magnet synchronous motor based on ring specimen test result. *IET Electric Power Applications* **13**, **9**, 1280–1286.

Kim, D.-M., Benoliel, P., Kim, D.-K., Lee T. H., Park, J. W. and Hong, J.-P. (2019b). Framework development of series hybrid powertrain design for heavy-duty vehicle considering driving conditions. *IEEE Trans*. *Vehicular Technology* **68**, **7**, 6468–6480.

Klein III, M. P. and Park, J. W. (2017). Effects of non-uniform temperature on in-situ current distribution and non-uniform state of charge measurements for $LiFePO_4$ and $LiNiMnCoO_2$ cells. *ECS Trans.* **77**, **11**, 81–97.

Lee, B.-H., Hong, J.-P. and Lee, J.-H. (2012). Optimum design criteria for maximum torque and efficiency of a line-start permanent-magnet motor using response surface methodology and finite element method. *IEEE Trans*. *Magnetics* **48**, **2**, 863–866.

Liu, C., Chai, K. K., Zhang, X., Lau, E. T. and Chen, Y. (2018). Adaptive blockchain-based electric vehicle participation scheme in smart grid platform. *IEEE Access*, **6**, 25657–25665.

Matsui, N., Takeda, Y., Morimoto, S. and Honda, Y. (2001). Design, and Control of IPMSM. *Ohmsha, Ltd.*

Momen, F., Rahman, K. and Son, Y. (2019). Electrical propulsion system design of Chevrolet bolt battery electric vehicle. *IEEE Trans*. *Industry Applications* **55**, **1**, 376–384.

Park, M.-R., Kim, H.-J., Choi, Y.-Y., Hong, J.-P. and Lee, J.-J. (2016). Characteristics of IPMSM According to Rotor Design Considering Nonlinearity of Permanent Magnet. *IEEE Trans*. *Magnetics* **52**, **3**, 1–4.

Rahman, K. and Hiti, S. (2017). Trends in EV propulsion components and systems [about this issue]. *IEEE Electrification Magazine* **5**, **1**, 2–3.

Search Term: Electric Vehicle (2019). Web of Science. http://www.webofknowlegde.com.

Wu, J., Wang, J., Gan, C., Sun, Q. and Kong, W. (2018). Efficiency optimization of PMSM drives using field-circuit coupled FEM for EV/HEV applications. *IEEE Access* **6**, 15192–15201.

Xiang, Z., Zhu, X., Quan, L. and Chen, Y. (2019). Design and analysis of double-air-gap flux-modulated permanent magnet motor considering leading working harmonics. *IEEE Trans*. *Magnetics* **55**, **6**, 1–5.

Xiong, R., Cao, J., Yu, Q., He, H. and Sun, F. (2017). Critical review on the battery state of charge estimation methods for electric vehicles. *IEEE Access*, **6**, 1832–1843.

Zhao, J., Fu, W., Zheng, Y., Chen, Z. and Wang, Y. (2019). Comparative study of modular-stator and conventional outer-rotor flux-switching permanent-magnet motors. *IEEE Access*, **7**, 38297–38305.